OPEN ACCESS Freely available online

ISSN 2737-5323
Volume 5, Issue 2
https://afm.iikii.com.sg
Applied Functional Materials

Article

Ballistic Performance Assessment of Advanced Composite Body Armors: An Experimental and Numerical Investigation

Numan Khan[1, 2]

[1] Department of Engineering, University of Campania "L. Vanvitelli", Aversa 81031, Italy, numan.khan@unicampania.it
[2] Department of Mechanical Engineering, University of Engineering and Technology, Peshawar 25000, Pakistan

Received: date; **Revised:** date; **Accepted:** date; **Published:** date

Abstract: Hybrid composites are widely utilized in body armor for security personnel, providing essential protection against ballistic threats. This study aims to investigate the ballistic performance of a body armor system comprising silicon carbide ceramic supported by Kevlar fiber-reinforced polymer (Kevlar-epoxy) using testing and numerical simulation. Finite element analysis was conducted to predict the failure mechanisms of bullet penetration by using a 7.62 × 51 mm hard steel core projectile and optimize the relative thicknesses of the armor components. The optimized design, consisting of 10 mm silicon carbide and 5 mm Kevlar composite, successfully stopped bullets corresponding to the National Institute of Justice (NIJ) threat level III. Samples of the optimized configuration were fabricated and tested according to the NIJ standards. Six shots were fired at each sample to evaluate the ballistic performance. The numerical model accurately predicted the failure modes induced by bullet impact. Results revealed that crack initiation, propagation, fracture conoid formation, and radial tensile cracks were the primary failure mechanisms in the ceramic layer, while progressive delamination and fabric breakage occurred in the polymeric composite. Increasing the thickness of the armor system reduced the bullet's velocity and kinetic energy, and an inverse relationship between composite thickness and the extent of delamination was observed. The measured backface signature was 22 mm, well within NIJ limits, and approximately 10% weight reduction per armor plate was achieved compared to existing systems of similar dimensions.

Keywords: Ballistic impact, Body armor, Numerical analysis, Composite materials, Silicon carbide

1. Introduction

Body armor is widely used by security personnel for their safety and protection. However, due to advancements in weapons and ammunition, there is a need for lightweight and effective body armor. Initially, monolithic metallic materials, including steel, titanium alloys, and aluminum, were widely used as body armor materials in most metallic armor systems. In principle, the hardness of the metallic target material is used to deform/erode the impactor, and ductility reduces the crack propagation in the target material under impact phenomena [1]. Similarly, the edge effect mechanism in perforated metallic armor increases the capability of of target material for the erosion and fragmentation of a projectile [1]. Although these metallic materials are efficient and economical, they are heavyweight, which limits their use in the body armor systems for prolonged use especially, in the arid, semi-arid, and arctic combat environments.

The limitations of metallic materials under impact loading require the exploration of ceramics and fiber-reinforced polymer composites, particularly in body armor, due to their superior strength-to-weight ratio and energy absorption capabilities [2–5]. Previous research results show that thermoplastic polymer performs better against the impact loading compared with thermoset polymers in fiber reinforced polymer composites [6,7]. Ceramics with high compressive strength and hardness are satisfactory materials for armor applications because of their relatively low densities [1]. For example, silicon carbide, alumina and boron carbide with high compressive strength and hardness perform effectively than metallic materials embedded in the armor system [8]. However, ceramics are brittle and shatter upon the impact of high-speed projectiles [9]. Therefore, a backing material of high strength is required to impede further penetration of bullet and absorption of its residual energy, leading to hybrid armor system [10,11]. Advancements in the hybrid body armor system have led to the development of fabric material such as Aramid (Kevlar), polyethylenem and e-glass, which show stronger behavior under ballistic loading conditions than the existing material [4,5,11,12]. Compared with metallic materials, these fabric materials absorb more impact energy transmitted from the bullet by each successive layer, thus reducing blunt trauma to the body of the wearer [13]. The impact resistance properties of the fabric material can be further enhanced by adding a hard material such as ceramic on the front-end side as mentioned earlier. Generally, in the design of

these composite body armor systems, the properties and thicknesses of individual component materials are considered. Furthermore, the performance of armor systems depends on the optimal thickness values and the interlayer bonding between the components.

Considerable progress in the hybrid armor system has been achieved by combining monolithic or tiled ceramics, composite backings, and polymeric interlayers to defeat high-energy projectiles [14–16]. These multilayered armor systems include ceramic strike faces for initial bullet breakage, composite backings for fragment arrest, and separating layers made from specialized ceramic-polymers. For example, ceramic with metallic backing [17] did not show an erosion of the projectile, as the energy to erode was higher than that used in ceramic fracture. Such advancements were not efficient in high-velocity range. James suggested an empirical model to quantify the ceramic-metal optimum thickness ratio and find the effect of the obliquity angle on target material under ballistic loadings [18]. Batra and Pydah [19] reported that adding a 2 mm thick polyether-ether-ketone (PEEK) surface layer to a SiC ceramic significantly reduced peak forces and pressure transmission during impact. Zhang *et al*. [20] demonstrated that prestressing ceramic tiles enhances projectile erosion, increasing the ballistic limit by over 25%. Similarly, Shen *et al*. [21] evaluated SiC/ ultra-high-molecular-weight polyethylene (UHMWPE) armor, showing that adhesive strength and material variability critically influence deformation and penetration.

In a composite body armor system, the ceramic component dissipates a major portion of projectile energy while the backing fiber-reinforced composite provides the structural support and acts as the load-carrying agent after the failure of the ceramic [22]. The primary sources for energy absorption in these systems are the radial crack formation, followed by tensile failure, heat generation, and ceramic pulverization. Chen *et al*. [11] compared the performance of hexagonal prism spherical crown ceramic/fiber composite plates against conventional ceramic/fiber composite plates of identical thickness. It introduces a novel composite armor design inspired by biological structures based on failure mechanisms, energy absorption capabilities, and the influence of geometric parameters on ballistic response. By employing multiple ceramic tiles separated by metal grids, the ballistic properties of armor were enhanced [23]. Pineapple leaf fiber (PALF) reinforced epoxy composites as a sustainable and cost-effective alternative to synthetic fibers for ballistic armor. The PALF composite's ability meets the NIJ standard and performs similarly to Dyneema, a widely used synthetic fiber. The potential of integrating PALF composites into hard armor upgraded ballistic vests from level IIIA to level III [24].

The backing composite material absorbs the residual energy through yarn compression, matrix cracking, fiber pullout, interlayer delamination, heat generation, and friction mechanisms [22]. Matrix cracking occurs as the mesoscale damage in fiber-reinforced polymers, whereas delamination is regarded as macroscale failure [25,26]. Karandikar *et al.* [27] described the inverse relationship between the fracture toughness and hardness of the ceramic used in armors. The hardness of the ceramic material contributes to the destruction of the bullet tip, while fracture toughness is responsible for providing the multi-hit ability of the body armor.

The ballistic properties of the ceramic materials can be enhanced by adding a strong backing material [28]. Crouch [29] emphasized the significance of ceramic materials in enhancing body armor effectiveness. He used ultra-high molecular weight polyethylene fibers and cladding materials to enhance the durability of hard armor plates. Krishnan *et al*. [30] reviewed the reinforcement of alumina (Al_2O_3) for the development of a reactive-sintering boron carbide (B_4C) matrix composite. These results collectively demonstrate the improvement of the mechanical properties and appropriateness of ceramic-based body armor for armor applications.

The optimum thickness of armor components is a critical design parameter, as both weight and cost are decisive factors in final material selection. For the ceramic front plate, increased thickness enhances projectile erosion capability but also adds weight, whereas reduced thickness compromises ballistic performance. Similarly, a relatively thick aramid backing layer is necessary for adequate ballistic protection; however, aramid is costly and labor-intensive to fabricate [31]. Accurate prediction of failure in hybrid armor systems with ceramic and polymeric components is essential for assessing their effectiveness [29]. While experimental studies are used to characterize these behaviors, sophisticated equipment, substantial material, and significant energy costs are required for repeated testing [29]. To mitigate these limitations, numerical simulations are used as an alternative method to explore failure mechanisms. Nevertheless, few numerical studies have reliably predicted penetration-induced failure modes, highlighting a need for research to reduce reliance on costly experimental trials in the armor design process.

In this study, ANSYS AUTODYN was used for ballistic penetration analysis, complemented by experiments, to predict failure modes in hybrid composite targets. SiC was selected as the ceramic front layer due to its exceptional hardness, high strength, low density, and proven ability to dissipate ballistic energy. These properties enable SiC to blunt and erode high-velocity projectiles, thereby reducing localized pressure on the backing layer and improving ballistic performance. Prior research [14–16,32–34] validated the use of SiC in multi-layer armor systems, particularly when paired with polymeric backings for high protection with optimized weight and thickness. Kevlar, an aramid fiber developed by DuPont, was chosen as the backing layer due to its high tensile strength-to-weight ratio, energy absorption capacity, and resistance to impact and penetration. When combined with SiC, Kevlar effectively dissipates residual projectile energy through mechanisms including fiber fracture, delamination, and pull-out.

The ceramic/Kevlar hybrid configurations offer an optimal balance of protection, weight, and flexibility, making them well-suited for personal body armor [15,35–37]. Based on the previous research results, Kevlar with SiC was evaluated for ballistic performance through experimental testing and numerical modeling in this study. The results of the simulation validated the numerical methodology, which provides a basis to design a body armor system optimized for thickness and capable of withstanding high-velocity projectile impacts. Live-fire ballistic test results also supported the optimized design, with results showing close agreement with the numerical predictions.

2. Materials and Methods

This section provides a detailed overview of the material specifications and the corresponding samples fabrication process, and explains the simulation model with the experimental procedure.

2.1 Target Sample

In target sample fabrication, a textile laminate composed of Kevlar fabric (DuPont, Pakistan) infused with Araldite epoxy and silicon carbide monolithic ceramics in the front face was employed as the backing layer. Kevlar sheets in dimensions of 254 mm × 305 mm with a thickness of 1 mm were prepared, conforming to the NIJ specifications [38]. The SiC ceramic plate of thickness 10 mm (supplied by China Hunan High Broad New Material Co. Ltd.), with a density of 3.16 g/cm³ and a shear modulus of 183 GPa [39], was used as the primary strike face material, while the Kevlar fabric, possessing a density of 1.44 g/cm³ and a tensile strength of 3.6 GPa [40] along the fiber direction, were used for absorbing energy. In the fabrication of the Kevlar–epoxy composite panel, a vacuum-assisted resin infusion technique was used to ensure uniform resin distribution and minimize void formation (Fig. 1). A symmetric [0/45/0] stacking sequence was adopted to enhance mechanical stability and reduce the risk of residual stresses or warping [41]. In infusion, Kevlar layers were arranged in a sealed vacuum bag system equipped with resin inlet and outlet ports, enabling controlled resin flow through a distribution medium. Following infusion, the panel was vacuum-cured for 24 hours and subsequently subjected to post-curing in a temperature-controlled furnace [42]. This secondary curing was conducted at 80–120 °C to promote optimal cross-linking of the epoxy matrix, thereby improving thermal resistance and interfacial bonding. The same bonding and curing procedure was applied to join the SiC plate to the Kevlar plate using Araldite epoxy. The combined effects of optimized layer orientation, vacuum-assisted resin infusion, and precise post-curing conditions significantly contributed to the laminate's structural integrity, reduced defect concentration, and enhanced mechanical performance. The fabricated Kevlar–epoxy plate is presented in Fig. 3(a), while the complete Kevlar–ceramic bonded target plate is shown in Figs. 3(b) and 3(c).

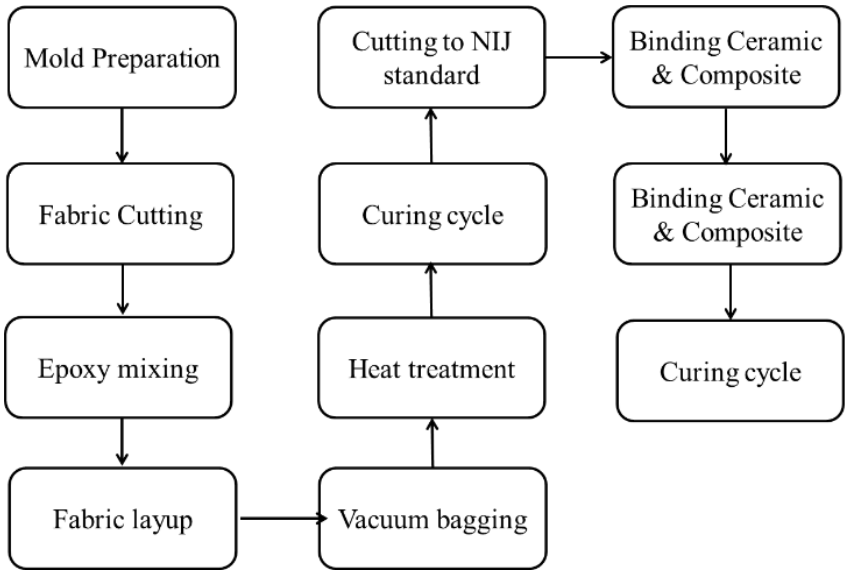

Fig. 1. Samples fabrication process.

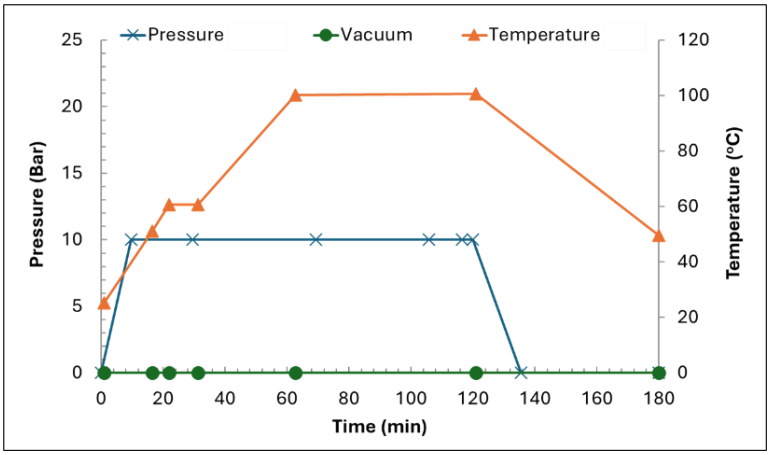

Fig. 2. Curing cycle for Kevlar-epoxy composite panel preparation.

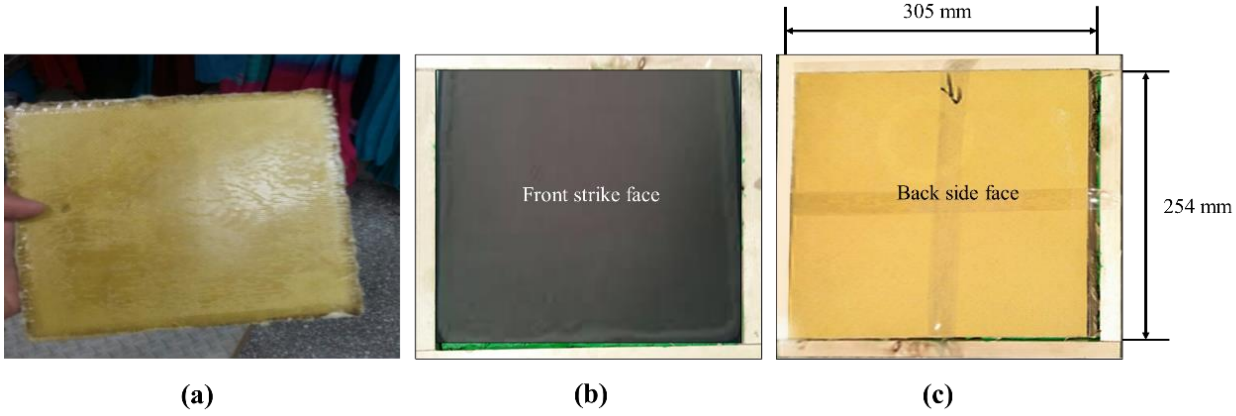

Fig. 3. (**a**) Fabricated Kevlar-epoxy composite plate (**b**) Front face (**c**) and back side (Kevlar-epoxy composite) of the test sample.

2.2 Ballistic Projectile Specifications

For threat level III, the ammunition 7.62 x 51 mm full metal jacket (FMJ), Armor-piercing (AP) steel (4340) core bullets with a specified mass of 9.6 g is used [27]. The bullet velocity of 820 ± 10 m/s was selected following the NIJ standard [38]. The dimensions of the bullet core are shown in Fig. 4.

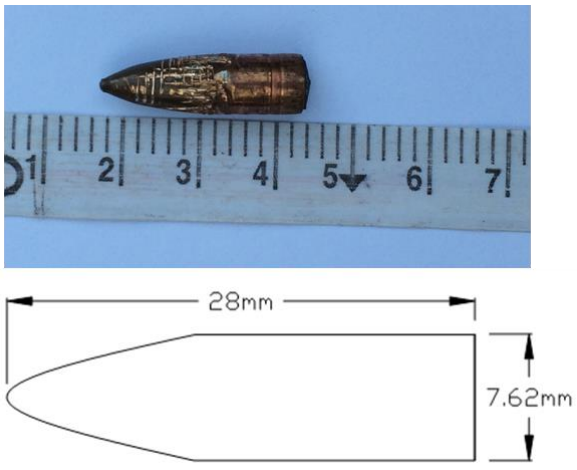

Fig. 4. 7.62 mm AP hardcore bullet and its dimensions.

2.3 Ballistic Test Experimental Set-Up

The schematic of the experimental setup is shown in Fig. 5, in which gun and target were positioned 15 m apart from each other. With a laser beam, the gun was set to aim at the center of the target. The projectile velocity was measured at two different instances during the flight of the projectile towards the target by employing an enhanced laser velocity sensor (ELVS) [43,44] based velocity measurement system (Fig. 5). ELVS adopts a 25.4 mm wide laser sheet aligned perpendicular to the projectile path. When the projectile passes the laser sheet the changing laser light intensity is recorded, and the velocity of projectile is calculated. Using this system, velocity up to about 1000 m/s was measured. In the experiment, six bullets were fired to determine the ballistic response of the armor plate. Roma plastilina modelling clay was used to measure backface signature (BFS) after the ballistic test at the backside of the armor system.

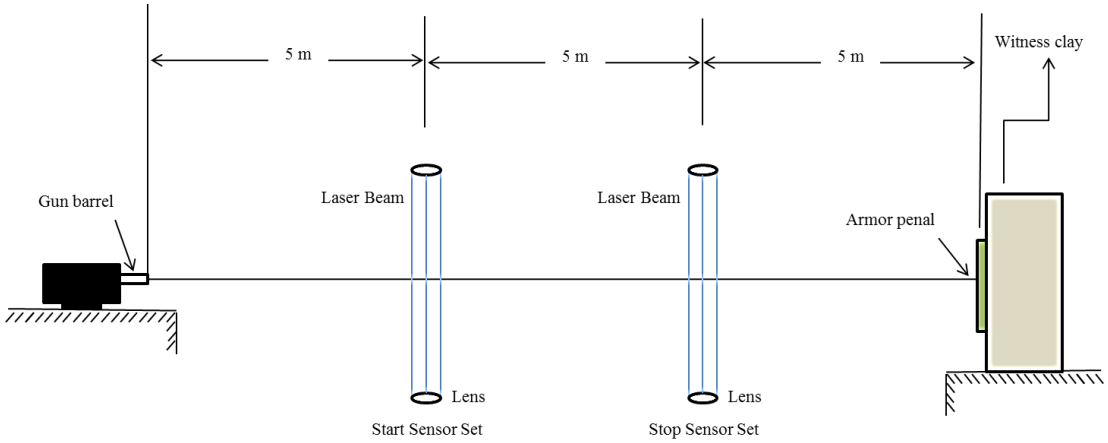

Fig. 5. Experimental setup used for ballistic test.

2.4 Simulation and Constitutive Laws

2.4.1 Meshing in Simulation

The finite element analysis was carried out using ANSYS AUTODYN, a robust solver for high-speed impact and nonlinear dynamic problems, utilizing explicit time integration to accurately capture the transient response during ballistic impact. The simulation was conducted to evaluate the penetration depth, stress wave propagation, damage morphology, and failure mechanisms induced by a high-velocity projectile, and the impact on the composite target. The dimensions and stacking sequence of the composite target plate were maintained identical to those used in the experimental setup to ensure model validity and facilitate direct comparison between simulation and physical testing.

In numerical modeling, the hardened steel 4340 core of the 7.62 mm armor-piercing bullet was considered. The copper jacket, significantly softer and known to disintegrate upon initial contact with hard ceramic surfaces, was not used in the simulation, as its contribution to the penetration process is minimal beyond the initial milliseconds [45]. This simplification allowed a more focused study on the core-target interaction while optimizing computational resources. To reduce computational time and memory demand without compromising accuracy, a quarter-symmetric model of the target and projectile was employed. In modeling, the symmetric nature of the physical system was considered in terms of geometry, loading conditions, and boundary constraints. Symmetry boundary conditions were applied along the symmetry planes (the *X-Z* and *Y-Z* planes) to simulate the 3D behavior with a reduced model domain. The final model configuration, mesh structure, and boundary conditions are illustrated in Fig. 6.

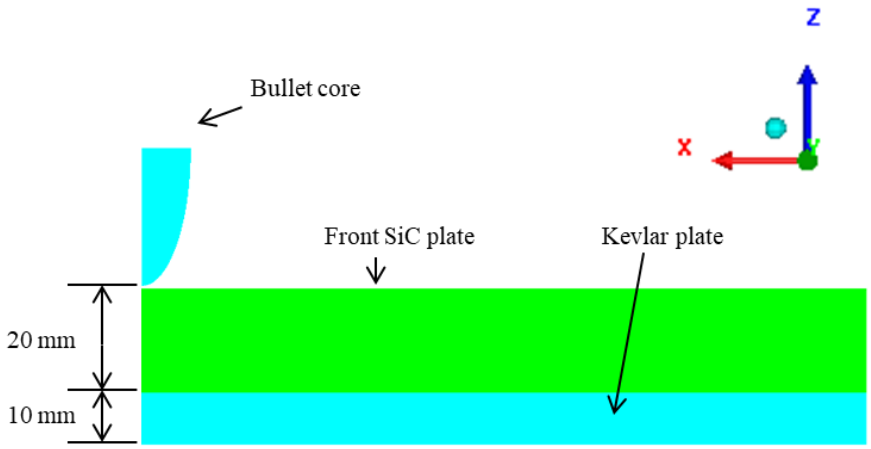

Fig. 6. Quarter symmetric finite element model of target composite material and bullet.

The meshing strategy for all numerical simulations was established based on a consistent methodology to ensure accuracy and comparability across configurations. In the finite element model, eight-noded linear hexahedral elements (SOLID164 in ANSYS AUTODYN) were included for the projectile and target materials, consistent with the approach in Ref. [46]. Radial mesh refinement was applied to the target plate, beginning at the projectile's impact zone and extending outward, to enhance computational stability and accurately capture the high-stress gradients near the impact site. This zoning approach enabled finer mesh resolution at the impact center and progressively coarser elements toward the plate edges, thereby balancing accuracy with computational efficiency. To capture the ballistic response of armor plates with varying thicknesses, mesh element size ranges were optimized for each configuration. The mesh density was adjusted according to the combined thickness of the SiC and Kevlar–epoxy layers, ensuring sufficient resolution in high-stress regions while maintaining computational efficiency. The mesh element size ranges and total element counts for both the target plate and projectile in each configuration are summarized in Table 1

Table 1. Summary of mesh element size ranges and total element counts for different SiC/Kevlar configurations used in the finite element simulations.

Configuration	Armor Plate Thickness (Mm)	Mesh Size Range (Mm)	Number of Elements in Target Plate	Number of Elements in Bullet
Preliminary case study	SiC = 20, Kevlar = 10	0.3–1.5	~270,000	~59,000
Config-1	SiC = 6 Kevlar = 3	0.25–1.3	~110,000	~59,000
Config-2	SiC = 8 Kevlar = 4	0.3–1.1	~160,000	~59,000
Config-3	SiC = 10 Kevlar = 5	0.3–1.3	~178,000	~59,000
Config-4	SiC = 12 Kevlar = 6	0.25–1.2	~196,000	~59,000

For predicting damage in hybrid silicon carbide-Kevlar composites under ballistic impact, constitutive models were integrated to capture brittle ceramic fracture, orthotropic delamination, and interfacial debonding. The Johnson-Cook (JC) model was employed to simulate the bullet's ductile deformation and failure by incorporating strain hardening, strain-rate sensitivity, and thermal softening effects. A damage variable (D) was used to track cumulative plastic strain, transitioning from undamaged ($D = 0$) to fully failed ($D = 1$) states, with element erosion at $D = 1$ to replicate material rupture. This was coupled with a Gruneisen equation of state to explore shockwave propagation and pressure effects during high-velocity impact. Similarly, the Johnson-Holmquist-II (JH-2) model was used to simulate SiC's dynamic fragmentation by incorporating pressure-dependent strength, strain-rate effects, and a damage variable (D) to transition from intact ($D = 0$) to fully fractured ($D = 1$) states, with element erosion at $D = 1$ to replicate catastrophic failure. This was combined with an orthotropic material model for Kevlar-epoxy, where delamination initiation was governed by the maximum through-thickness tensile ($\varepsilon 33$) and shear ($\varepsilon 13$, $\varepsilon 23$) strains, followed by progressive stiffness degradation in simulating interlaminar bond weakening. The SiC-Kevlar interfacial debonding was employed as an erosion criterion (critical

geometric strain = 1.2) to remove elements at the interface, ensuring computational stability under high-strain-rate loading. A surface-to-surface contact algorithm [47], augmented by nodes-to-surface tracking, modeled projectile-target interaction, preventing penetration and enabling progressive degradation of contact forces aligned with SiC's brittle fracture and Kevlar's fiber-matrix decohesion. The synergy of JC for Steel, JH-2 for SiC comminution, orthotropic damage for Kevlar ply failures, and erosion-based debonding enabled capturing holistic failure progression, penetration depth, and fracture patterns. This multi-model approach is a robust tool for analyzing impact-resistant ceramic-composite armor systems (Fig. 7).

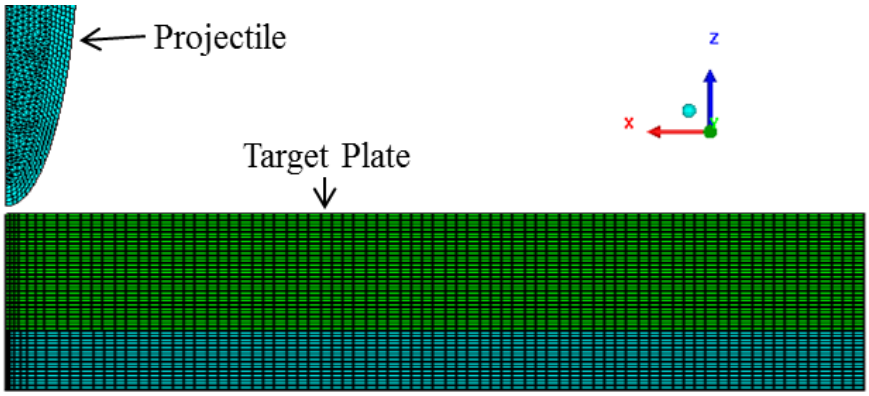

Fig. 7. Quarter meshed model of the target plate.

2.4.2 Constitutive Law for Projectile

The Johnson-Cook (JC) material and damage model [48] is commonly used as a constitutive model for metallic materials in ballistic research. It is frequently used in ballistic science and engineering as a viscoelastic model and has been developed based on experimental data at various strain rates and temperatures. The JC model is given by equation (1).

$$\sigma_Y = (A + B\varepsilon^n)(1 + C\ln\varepsilon^*)(1 - T^{*m}] \quad (1)$$

where σ_Y is the dynamic yield strength, and A, B, C, n, m are material constants, while T* is the homologous temperature when determining these constants. In addition to the material behavior model (constitutive law), an equation of state (EOS) is used to define the relationship among the hydrostatic pressure, the local density, and local specific energy. In the numerical model of this study, the Gruneisen EOS was used (equation (2)) [49].

$$P = \frac{\rho_0 C_{sp}^2\left[1+\left(1-\frac{\gamma_0}{2}\right)\mu-\frac{a}{2}\mu^2\right]}{\left[1-(S_1-1)\mu-S_2\frac{\mu^2}{\mu+1}-S_3\frac{\mu^3}{(\mu+1)^2}\right]} + (\Gamma_0 + a\mu)E_{int} \quad (2)$$

where P represents pressure, C_{sp} is the intercept of the vs-vp curve, Γ_0 is a Grüneisen coefficient, and μ is defined as $\mu = \frac{\rho}{\rho_0} - 1$. In addition to the EOS and constitutive law, the damage model was used to explore the accumulation of damage as a function of increasing load. Accordingly, the JC damage model based on the accumulative plastic strain and failure was employed when the damage parameter exceeded 1. *D* was used as a scalar quantity and was computed using equation (3) [48].

$$D = \sum \frac{\Delta\varepsilon^p}{\varepsilon_f^p} \quad (3)$$

where $\Delta\varepsilon^p$ is the plastic equivalent strain (a scalar quantity), and ε_f^p is the ultimate plastic strain expressed as in equation (4).

$$\varepsilon_f^p = [D_1 + D_2\exp(D_3\sigma^*)]\left[1 + D_4\ln\left(\frac{\dot{\varepsilon}_{pl}}{\dot{\varepsilon}_0}\right)\right]\left[1 + D_5\left(\frac{T-T_R}{T_M-T_R}\right)^m\right] \quad (4)$$

Equation (4) defines the material crack locus in terms of stress triaxiality, represented by σ*, which is defined as the ratio of hydrostatic pressure to Von-Mises stress. Analogous to the strength model, the damage model within the JC formulation distinguishes between temperature and strain effects, incorporating specific damage coefficients such as D_1, D_2, D_3, D_4, and D_5. The constant parameters of the metallic bullet core (4340 steel) utilized in the simulation, as per the JC material model, were obtained as listed in Table 2 [50].

Table 2. JC strength and damage model constants for 4340 steel core bullet.

Density, ρ (g/cm^3)	Shear Modulus (Gpa)	Strength Constants

		A (Gpa)	B (Gpa)	N	C	M
7.85	78	0.910	0.586	0.26	0.014	1.03
Damage Constants						
D_1	**D_2**	**D_3**	**D_4**		**D_5**	
-0.8	2.1	-0.5	0.002		0.61	
Mie–Gruneisen Equation of State Constants						
Γ_0	**C1 (m/s)**		**S_1**		**T_{ref} (K)**	
1.16	3574		1.91		300	

2.4.3 Constitutive Law: Ceramic plate

To accurately model the behavior of the ceramic plate, the JH-II model [51] was employed to replicate the brittle nature of the ceramic material. A polynomial equation of state was utilized to establish a correlation between pressure, volumetric change, and compressibility modulus. Equation (5) [52] defines material stress (σ^*) under high strain rate and high-pressure conditions by adjusting parameters such as intact strength (σ_i^*), fracture strength (σ_f^*), and damage parameter (D).

$$\sigma^* = \sigma_i^* - D(\sigma_i^* - \sigma_f^{*\cdot}) \quad (5)$$

The normalized intact stress (σ_i^*) and fractures stress (σ_f^*) is defined in equations (6) and (7), respectively.

$$\sigma_i^* = A(P^* + T^*)^N (1 + C \ln \varepsilon^*) \quad (6)$$
$$\sigma_f^* = B(P^*)^M (1 + C \ln \varepsilon^*) \quad (7)$$

where A, B, C, M, and N are material constants, P* is the normalized pressure, T* is the normalized hydrostatic tension, and ε* is the dimensionless strain rate. The polynomial equation of state is given as equation (8) [53].

$$P_{HEL} = K_1\mu + K_2\mu^2 + K_3\mu^3 \quad (8)$$

where the compressibility factor $\mu = \frac{\rho}{\rho_0} - 1$ with ρ current density, ρ_0 reference density of material while K_1, K_2, K_3 are material constants. Similarly, stresses at Hugoniot Elastic limit (HEL, σ_{HEL}) is calculated using equation (9).

$$\sigma_{HEL} = \frac{3}{2}(HEL - P_{HEL}) \quad (9)$$

Similar to the JC model, the JH-II model's damage variable is expressed in terms of plastic strain expressed by equation (10).

$$D = \sum \frac{\Delta\varepsilon^p}{\varepsilon_f^p} \quad (10)$$

where $\Delta\varepsilon^p$ = increment of plastic strain, ε_f^p = plastic strain at fracture, it is a function of the actual pressure given by equation (11) [53].

$$\varepsilon^f = D_1(P^* + T^*)^{D_2} \quad (11)$$

where *A, B, C, M, N, T, HEL, D_1 and D_2* are constants adopted from Ref. [39] (Table 3).

Table 3. Johnson-Holmquist strength and damage model constants for SiC.

Density, (g/cm^3)	**Shear Modulus, (GPa)**	**Strength Constants**				
		A (GPa)	**B (GPa)**	**N**	**C**	**M**
3.16	183	0.96	0.35	0.65	0	1
Damage Constants						
D_1				**D_2**		
0.48				0.48		
Equation of State Constants						
K1 (Bulk Modulus, (GPa)		**K2 (GPa)**		**K3 (GPa)**		**ß (Beta)**
204.78		0		0		1
Ref Strain Rate	Tensile strength (GPa)	Normalized Fracture Strength (GPa)	HEL (GPa)	HEL Pressure (GPa)	HEL Vol. Strain (μ)	HEL Strength (GPa)
1	0.37	0.8	14.567	5.9	0.0242	13

2.4.4 Constitutive Law: Composite plate

The composite plate, comprising continuous Kevlar and epoxy, was simulated using an orthotropic material model, which accounts for various complex phenomena including material anisotropy, vaporization, decomposition, melting, and anisotropic strength degradation. This model combines volumetric and deviatoric responses to high-velocity ballistic impacts. The behavior of orthotropic materials is described by constitutive relations based on stress-strain formulations, as outlined in equation (12) [54].

$$[\sigma]^{n+1} = [\sigma]^{n} + [C][\dot{\varepsilon}]\,\Delta t \tag{12}$$

where $[C]$ is the stiffness matrix determined from the elastic constants in material principal directions, $[\dot{\varepsilon}]$ is the strain rate tensor, and Δt stands for the time step. The maximum strain criterion is used for damage initiation, while progressive damage analysis is conducted for damage evolution. To distinguish the thermodynamic EOS response of the material from its ability to bear the shear loads, it is appropriate to separate strains into their average (ε_{avg}) and deviatoric (ε_{ij}^{d}) components. The total strain tensor is thus rendered in equation (13).

$$\varepsilon_{ij} = \varepsilon_{ij}^{d} + \varepsilon_{avg} \tag{13}$$

For an orthotropic material, the Mie–Gruneisen EOS and correction factor due to deviatoric strains are formulated as shown in equation (14) [55].

$$P = P_{r(\varepsilon_{vol})} + \frac{\Gamma_{(v)}}{v}[e_r - e_{r(\varepsilon_{vol})}] + \text{correction factor} \tag{14}$$

where $P_{r(\varepsilon_{vol})}$ and $e_{r(\varepsilon_{vol})}$ define material pressure-volume and energy–volume connection with reference to the shock Hugoniot. The Grüneisen gamma $\Gamma_{(v)}$, a thermodynamic property of a material is used to extrapolate the material states off the reference to the Hugoniot shock. Material constants for the orthotropic material mode for Kevlar-epoxy composite adopted from Ref. [40] (Table 4).

Table 4. Material and damage constants for Kevlar-Epoxy plates.

Property	Unit	Value
Density (ρ)	g/cm^3	1.65
Ortho equation of State (EOS) Constants		
Fiber direction Young's Modulus (E_{11})	GPa	17.989
Transverse direction Young's Modulus (E_{22})	GPa	17.989
Transverse direction Young's Modulus (E_{33})	GPa	19.48
Poisson's ratio (ν_{12})	--	0.08
Poisson's ratio (ν_{23})	--	0.698
Poisson's ratio (ν_{31})	--	0.0756
Shear Modulus (G_{12})	GPa	1.857
Shear Modulus (G_{23})	GPa	0.223
Shear Modulus (G_{31})	GPa	0.223
Failure (Stress/ Strain) Constants		
Tensile failure strain (ε_{11}^{f})	--	0.06
Tensile failure strain (ε_{22}^{f})	--	0.06
Tensile failure strain (ε_{33}^{f})	--	0.02
Post-Failure Options		**Orthotropic**
Residual shear stiffness friction	--	0.02
Failed in 11, failure mode	--	11 only
Failed in 22, failure mode	--	22 only
Failed in 33, failure mode	--	33 only
Failed in 12, failure mode	--	12 and 33 only
Failed in 12, failure mode	--	23 and 33 only
Failed in 12, failure mode	--	31 and 33 only

3. Results and Discussion

3.1 Preliminary Validation

Bullet impact on target materials is a complex phenomenon, and capturing the penetration mechanisms and subsequent failure modes during impact requires a challenging experimental setup. Alternatively, the penetration process and optimization of the target are studied using numerical simulations. Nevertheless, the results of the numerical simulation need to be supplemented with experimental validation. To validate the numerical model accuracy, a case study of bullet target penetration was performed in this study, in which a 30 mm thick target plate (20 mm SiC backed by 10 mm Kevlar-epoxy composite) was fabricated and tested in the ballistic test range. The bullet velocity of 820 $\pm$ 10 m/s was selected according to the NIJ standard [38]. Then, numerical simulations were performed by keeping the target material and thickness similar to the experimental setup. The post-test sample shown in Fig. 8. The damage formation, hole penetration area, and failure type were determined in the experiment and simulation, whose results were similar. As shown in Fig. 8(b), the bullet was captured by the Kevlar-epoxy plate, preventing penetration in the armor material system.

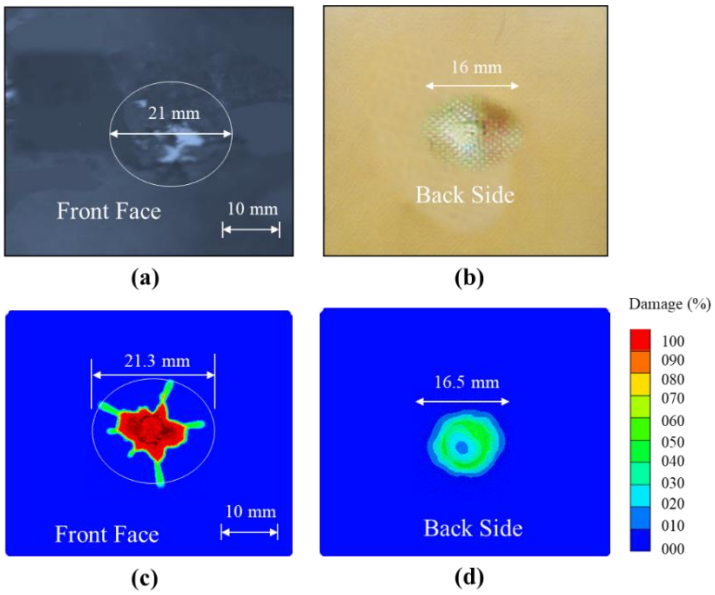

Fig. 8. Damage comparison, (**a**) radial cracks and fragmentation in the front ceramic plate, (**b**) BFS in Kevlar-epoxy composite (partial penetration), (**c**) numerical prediction of damage in ceramic, (**d**) BFS in Kevlar-epoxy composite.

The BFS of 30 mm target material after the impact was measured using the Roma plastilina modelling clay and was compared with simulated values. A maximum BFS value of 6.8 mm was observed based on the experimental results, while the simulated value was 6 mm (Fig. 9).

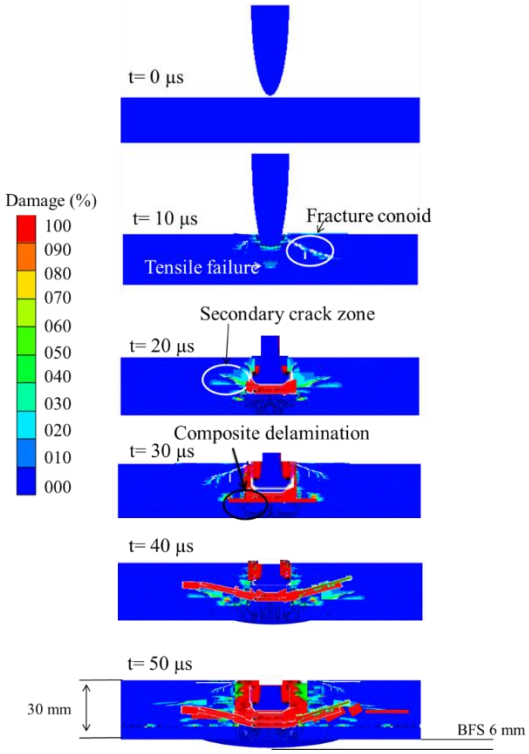

Fig. 9. Simulation results of failure mechanisms in target test material (BFS of 6 mm is clearly shown).

Damage in the plate initiated within the contact zone in which elements lost all residual strength, being eroded once the damage value reached the critical threshold defined by the damage accumulation law. The onset and progression of damage in the target plate at various penetration stages are illustrated in Fig. 9. Crack initiation in the ceramic layer was observed shortly after impact, at approximately 5 µs, accompanied by blunting of the projectile tip due to erosion of the hard ceramic surface. At 11 µs, a fracture conoid and tensile failure were observed. Conoid formation is a common ceramic failure under compressive loading, arising from the distribution of localized stresses over a broader area. Propagation of the fracture conoid generated radial cracks in the ceramic, which coincides with observations in Ref. [56]. The tensile failure was attributed to the reflection of tensile stress waves at the ceramic–composite interface. As penetration progressed, delamination within the composite backing was observed at approximately 29 µs, caused by shear stress development between composite layers. This damage mechanism absorbed a significant portion of the projectile's kinetic energy. Notably, the projectile was completely blunted by the ceramic strike face, halting further penetration by the end of the impact event, as shown in Fig. 10. The results validated the simulation model in this study. The results of the simulation and experiments coincided in terms of BFS, failure mechanisms, bullet erosion, and fracture conoid formation. The results aligned with previous ones [34,56]. Therefore, the same models can be used to optimize the dimensions of an efficient body armor system and minimize weight while enhancing ballistic performance.

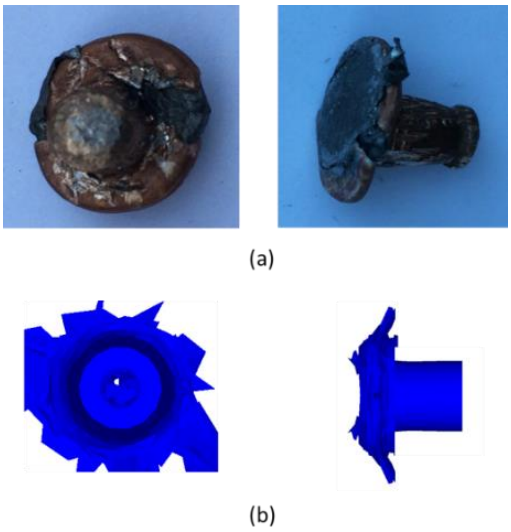

Fig. 10. Post-impact bullet topology, (**a**) experiment, (**b**) simulation.

3.2 Body Armor Design Simulation

Numerical simulations for four different configurations of the proposed armor system were performed at a strike velocity of 820 ± 10 m/s [38]. The composite armor thickness ratio of 2 was kept for all different cases [57], as shown in Table 5.

Table 5. Ceramic-composite thickness selected for simulation.

Configuration Number	Ceramics Plate Thickness (mm)	Kevlar-Epoxy Plate Thickness (mm)
1	6	3
2	8	4
3	10	5
4	12	6

The different penetration stages in the target material at the end of the simulation are shown in Fig. 11. The target of configuration 1 was completely penetrated (Fig. 11(a)), while that of configuration 2 was partially penetrated by the bullet (Fig. 11b). By increasing the thickness value of the target material in configurations 3 and 4 (Fig. 11(c) and (d)), it stopped the penetration. Various types of failures occurred in the target plate due to the bullet impact at a high velocity, as observed in the case study. The higher degree of damage was induced in configurations 1 and 2, compared with configurations 3 and 4. The bullet has penetrated with the complete failure of both the ceramic and composite parts of target materials in configurations 1 and 2, while partial damage was produced in configurations 3 and 4. The formation of the fracture conoid at the start of the simulation at =12 μs caused radial cracks, and tensile failure occurred due to the reflected shock waves in all cases. The fracture conoid failure in the ceramic material became more visible as the bullet penetrated further. The delamination in the composite occurred at 19 μs, when an inverse relation of delamination damage level to the thickness of the fabric composite backing material was observed. With the increase in the backing plate thickness, delamination decreased due to the higher resistance to plugging and greater delamination area, which was observed by Cristescu *et al*. [58]. In addition to delamination failure, the fiber breakage of the composite was also found.

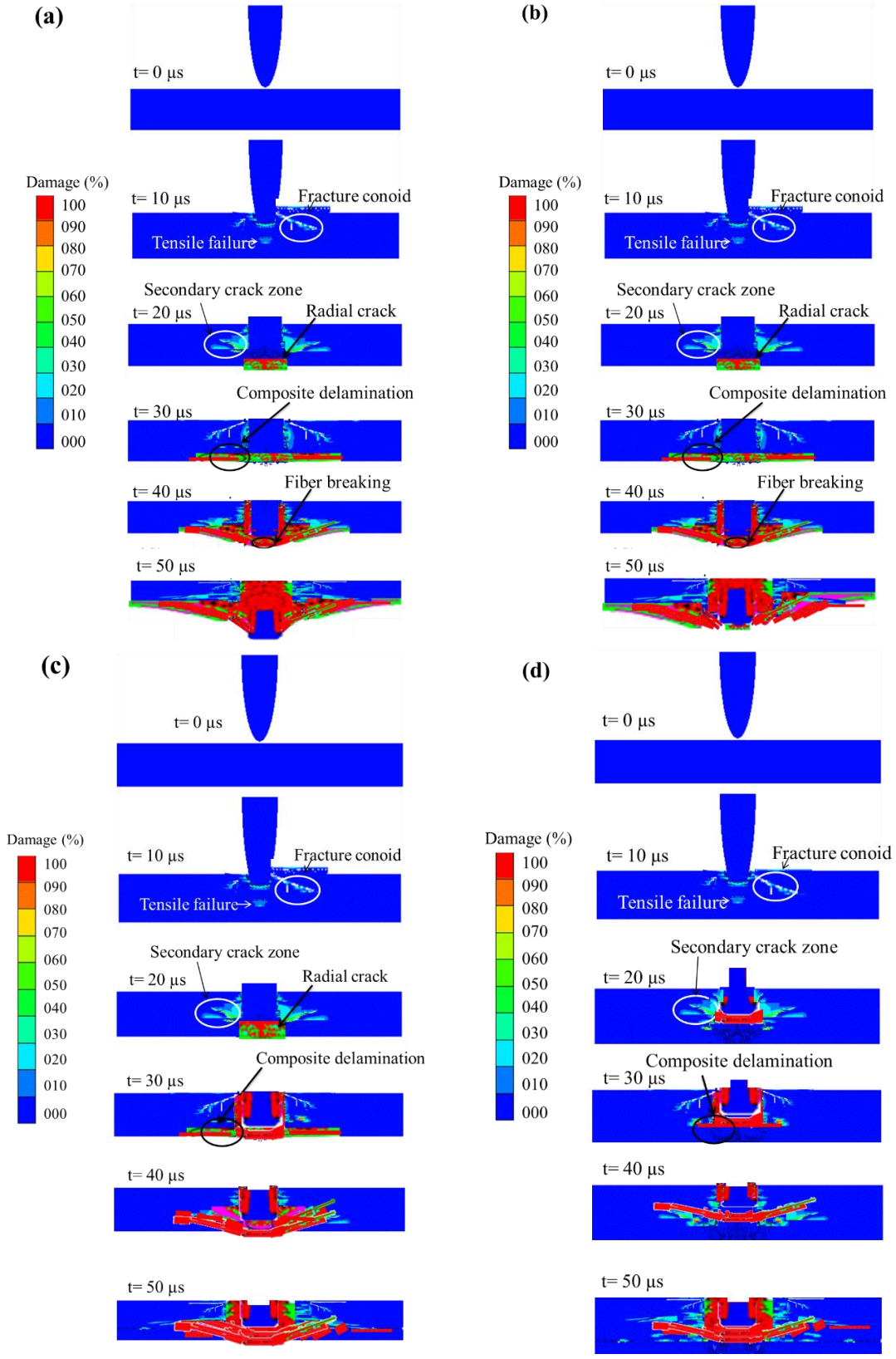

Fig. 11. Target material failure modes, (**a**) configuration 1 (6 mm SiC, 3 mm Kevlar composite), (**b**) configuration 2 (8 mm SiC, 4 mm Kevlar composite), (**c**) configuration 3 (10 mm SiC, 5 mm Kevlar composite), (**d**) configuration 4 (12 mm SiC, 6 mm Kevlar composite).

The decrease in the velocity of the bullet during the penetration in the simulation was plotted against the time (Fig. 12). The bullet showed a residual velocity of about 180 m/s in configuration 1 (through penetration), while the residual velocity was 82 m/s

at the end of the simulation time (configuration 2). The bullet penetrates the target material in configuration 2. Furthermore, bullet velocity was reduced to zero at the end of the simulation time with an increase in the target thickness. In configuration 4, the bullet was stopped at 34 µs, compared with 42 µs in configuration 3.

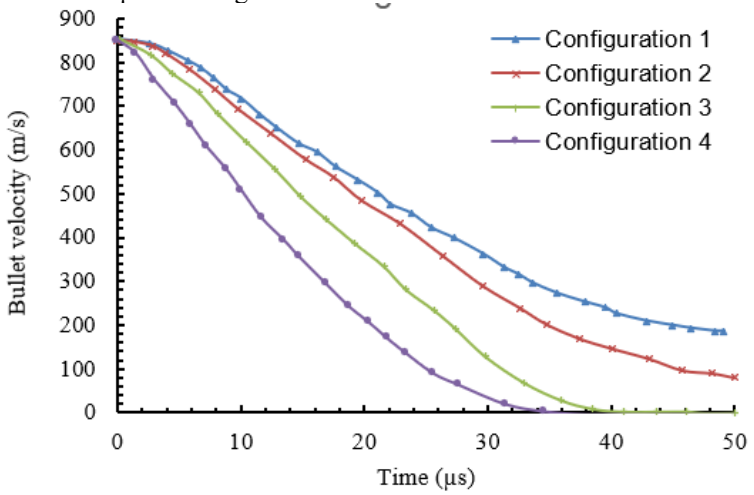

Fig. 12. Drop-in bullet velocity for the four different configurations.

The bullet kinetic energy drop is shown in Fig. 13. The drop in kinetic energy increased with an increase in target material thickness, as a more rapid drop of kinetic energy was observed in configurations 3 and 4. As the bullet was stopped in configurations 3 and 4, the kinetic energy of the bullet became zero at 27 and 34 µs, respectively, while the bullet had sufficient residual kinetic energy in configurations 1 and 2. In configurations 3 and 4, higher ballistic performance was observed than in configurations 1 and 2. Considering a lighter weight and lower costs, configuration 3 is appropriate, with 10 mm Silicon carbide backed by 5 mm Kevlar-epoxy composite. Configuration 3 provided sufficient ballistic protection against the NIJ threat level III.

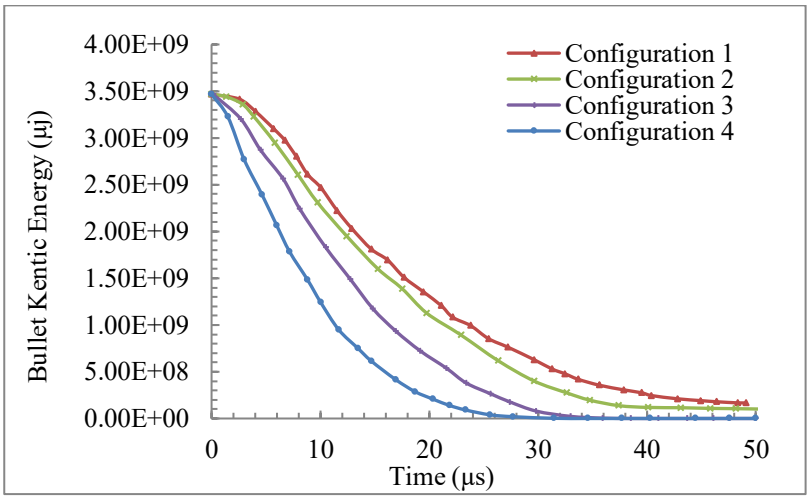

Fig. 13. Kinetic energy drop of the bullet for different configurations.

3.3 Testing Ballistic Performance

Ballistic testing was carried out on three different samples, each fabricated according to configuration 3. Six separate shots were fired at each sample, following the NIJ 0101.06 standard for ballistic testing. In testing, the performance of the armor system was evaluated, and BFS was measured to estimate the bullet impact. In numerical simulation results, configuration 3 was considered the best as it demonstrated its superior ballistic performance, particularly in terms of velocity drop and kinetic energy dissipation (Figs. 12 and 13). Given its promising results in simulations, configuration 3 was selected for experimental testing to verify its real-world performance.

Three samples with identical configurations and thickness ratios were tested to evaluate uncertainties and potential variations in the manufacturing process and experimental procedures, as minor differences might influence ballistic performance; therefore,

testing multiple samples enhances the reliability and representativeness of the results. To measure BFS, Roma Plastilina modeling clay was placed on the rear face of each armor sample to record the depth of indentation caused by projectile impact (Fig. 14) so that the armor's ability to stop a bullet could be evaluated while limiting backface deformation, which is critical for reducing the risk of blunt trauma to the wearer. Although variations in impact velocity among the three samples were minimal, they showed inherent variability in experimental conditions. The results captured the full range of possible performance outcomes, thereby improving the robustness and consistency.

The maximum BFS was 22 mm, while numerical simulations predicted 20 mm (Table 6). Both values were below the NIJ 0101.06 maximum BFS of 44 mm, confirming that the proposed armor system based on configuration 3 meets the standard's safety requirements. These results demonstrated that the system provides effective ballistic protection while maintaining a BFS significantly below the critical threshold, ensuring its suitability as a reliable armor solution. Repeated test results confirmed configuration 3's superior ballistic performance in accordance with NIJ standards, strengthening confidence in the design's ability to perform consistently under varying experimental conditions.

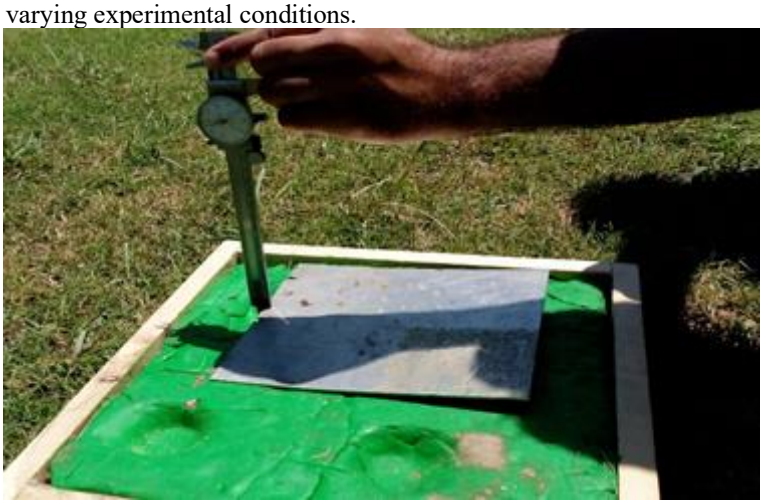

Fig. 14. BFS measurement using Roma plastilina modelling clay.

Table 6. Comparison of experimental and numerical results for ballistic testing of three test samples.

Test number	Shot number	Bullet strike velocity (m/s)		BFS (mm)		Perforation
		Experiment	Simulation	Experiment	Simulation	
Test sample 1	1	820	820	22	20	No
	2	818	818	20	20	No
	3	817	817	19	18	No
	4	817	817	21	19	No
	5	818	818	18	18	No
	6	814	814	19	17	No
Test sample 2	1	813	813	13	15	No
	2	815	815	15	17	No
	3	812	812	12	16	No
	4	810	810	16	18	No
	5	820	820	15	17	No
	6	818	818	14	19	No
Test sample 3	1	817	817	13	19	No
	2	817	817	17	14	No
	3	818	818	18	19	No
	4	814	814	17	14	No
	5	813	813	14	15	No
	6	819	819	13	19	No
Average		816	816	16	17	No

4. Conclusions

The combination of ceramics with woven fiber-reinforced polymer composites, particularly with Kevlar woven fabrics, enables a highly effective material system for enhanced ballistic performance with reduced weight. In this study, a body armor design was developed, and its ballistic protection capability against NIJ Threat Level III projectiles was verified through simulations and tests. The explicit simulation was conducted to validate in a case study and compared with experimental results. The adopted model successfully predicted the complex failure mechanisms in cladded ceramic and Kevlar fiber-reinforced polymer composites. In addition to replicating failure modes, the simulations accurately predicted perforation growth and projectile penetration behavior in both ceramic and composite layers under impact loading, showing close agreement with experimental observations. The results indicated that increasing the overall armor thickness significantly reduced the projectile's residual velocity and, consequently, its remaining kinetic energy. The simulation results showed an inverse relationship between the thickness of the Kevlar fiber-reinforced polymer backing and the extent of delamination. Compared with conventional body armor solutions, the proposed design achieved an approximate 10% weight reduction without compromising protection. Based on the results, the ceramic front plate with a composite backing is recommended for personal and structural protection, as the best configuration showed superior energy absorption and the propagation mitigation of shock-wave-induced cracks.

Funding: This research did not receive external funding

Informed Consent Statement: Not applicable

Data Availability Statement: Not applicable

Conflicts of Interest: The author declares no conflict of interest.

References

1. Hazell, P.J. *Ceramic Armour: Design and Defeat Mechanisms*. Argos Press: Canberra, Australia, 2006.
2. Aamir, M.; Tolouei-Rad, M.; Giasin, K.; et al. Recent advances in drilling of carbon fiber–reinforced polymers for aerospace applications: A review. *The International Journal of Advanced Manufacturing Technology* **2019**, *105*, 2289–2308. https://doi.org/10.1007/s00170-019-04348-z
3. Sadanandan, S.; Hetherington, J.G. Characterisation of ceramic/steel and ceramic/aluminium armours subjected to oblique impact. *International Journal of Impact Engineering* **1997**, *19*, 811–819. https://doi.org/10.1016/S0734-743X(97)00009-8
4. Berk, B.; Karakuzu, R.; Toksoy, A.K. An experimental and numerical investigation on ballistic performance of advanced composites. *Journal of Composite Materials* **2017**, *51*, 3467–3480. https://doi.org/10.1177/0021998316689877
5. Abtew, M.A.; Boussu, F.; Bruniaux, P.; et al. Ballistic impact mechanisms – A review on textiles and fibre-reinforced composites impact responses. *Composite Structures* **2019**, *223*, 110966. https://doi.org/10.1016/j.compstruct.2019.110966
6. Ud Din, I.; Caron, J.-F.; Toussaint, F.; et al. Finite element modeling of indentation and adhesive wear in sliding of carbon fiber reinforced thermoplastic polymer against metallic counterpart. *Tribology International* **2019**, *135*, 200–212. https://doi.org/10.1016/j.triboint.2019.02.046
7. Shah, S.Z.H.; Megat-Yusoff, P.S.M.; Karuppanan, S.; et al. Compression and buckling after impact response of resin-infused thermoplastic and thermoset 3D woven composites. *Composites Part B: Engineering* **2021**, *207*, 108592. https://doi.org/10.1016/j.compositesb.2020.108592
8. Rosenberg, Z.; Dekel, E.; Hohler, V.; et al. On the main mechanisms for defeating AP projectiles, long rods and shaped charge jets. *International Journal of Impact Engineering* **2009**, *36*, 588–596. https://doi.org/10.1016/j.ijimpeng.2008.09.004
9. Grujicic, M.; Pandurangan, B.; Koudela, K.L.; et al. A computational analysis of the ballistic performance of light-weight hybrid composite armors. *Applied Surface Science* **2006**, *253*, 730–745. https://doi.org/10.1016/j.apsusc.2006.01.019
10. Horsfall, I.; Buckley, D.H. The effect of through-thickness cracks on the ballistic performance of ceramic armour systems. *International Journal of Impact Engineering* **1996**, *18*, 309–318. https://doi.org/10.1016/0734-743X(95)00046-8
11. Chen, J.; Li, X.; Zhang, R.; et al. Lightweight Design and Experimental Study of Ceramic Composite Armor. *Materials* **2022**, *10*, 1056. https://doi.org/10.3390/ma10061056
12. Deniz, T. *Ballistic Penetration of Hardened Steel Plates*. Master Thesis, Middle East Technical University, Ankara, Turkey, 2010.
13. Regassa, Y. Modeling and Simulation of Bullet Resistant Composite Body Armor. [Preprint] Available online: https://doi.org/10.20944/preprints202203.0120.v1 (accessed on June 18, 2025).
14. Yadav, S.; Ravichandran, G. Penetration resistance of laminated ceramic/polymer structures. *International Journal of Impact Engineering* **2003**, *28*, 557–574. https://doi.org/10.1016/S0734-743X(02)00107-4
15. Saleem, I.A.; Ahmed, P.S.; Abed, M.S. Experimental and numerical investigation of Kevlar and UHMWPE multi-layered armors against ballistic impact. *Materials Today: Proceedings* **2022**, *56*, 2516–2524. https://doi.org/10.1016/j.matpr.2021.11.589

16. Tan, P. Finite element simulation of the behaviours of laminated armour systems against blast wave and projectile dynamic impacts. *Proceedings of the Institution of Mechanical Engineers, Part L: Journal of Materials: Design and Applications* **2013**, *227*, 2–15. https://doi.org/10.1177/1464420712452247
17. Mayseless, M.; Bogoch, A.; Keown, M.; Walker, J.D. Impact on ceramic targets. *Journal of Applied Mechanics* **1987**, *54*, 373–378. https://doi.org/10.1115/1.3173037
18. James, B.J. Practical issues in ceramic armour design. In *Ceramic Armor Materials by Design*; McCauley, J.W., Ed.; John Wiley & Sons: Hoboken, NJ, USA, 2002; pp. 33–44.
19. Batra, R.; Pydah, A. Impact analysis of PEEK/ceramic/gelatin composite for finding behind the armor trauma. *Composite Structures* **2020**, *237*, 111863. https://doi.org/10.1016/j.compstruct.2020.111863
20. Zhang, R.; He, L.; Zhao, X.; Guan, Z. Influence of prestress on ballistic performance of bi-layer ceramic composite armors: experiments and simulations. *Composite Structures* **2019**, *227*, 111258. https://doi.org/10.1016/j.compstruct.2019.111258
21. Shen, Z.; Yu, X.; Li, Y.; Feng, F.; Li, J. Ballistic reliability study on SiC/UHMWPE composite armor against armor-piercing bullet. *Composite Structures* **2019**, *213*, 209–219. https://doi.org/10.1016/j.compstruct.2019.01.090
22. Naik, N.K.; Shrirao, P.; Reddy, B.C.K. An energy-based model for ballistic impact analysis of ceramic-composite armors. *International Journal of Damage Mechanics* **2012**, *22*, 145–187. https://doi.org/10.1177/1056789511435346
23. Yang, L.; Wang, Z.; Zhou, C.; Liu, Y.; Huang, F. Ballistic performance of composite armor with dual layer piecewise ceramic tiles under sequential impact of two projectiles. *Mechanics of Advanced Materials and Structures* **2022**, *29*, 1–14. https://doi.org/10.1080/15376494.2020.1839605
24. Luz, F.S.d.; Garcia, F.d.C.; Oliveira, M.S.; Nascimento, L.F.C.; Monteiro, S.N. Composites with natural fibers and conventional materials applied in a hard armor: A comparison. *Polymers* **2020**, *12*, 1920. https://doi.org/10.3390/polym12091920
25. Ud Din, I.; Caron, J.-F.; Toussaint, F.; Jochum, C. Elastoplastic CDM model based on Puck's theory for the prediction of mechanical behavior of Fiber Reinforced Polymer (FRP) composites. *Composite Structures* **2018**, *201*, 291–302. https://doi.org/10.1016/j.compstruct.2018.06.047
26. Ud Din, I.; Caron, J.-F.; Toussaint, F.; Jochum, C. Sequential damage study induced in fiber reinforced composites by shear and tensile stress using a newly developed Arcan fixture. *Journal of Materials Research and Technology* **2020**, *9*, 13352–13364. https://doi.org/10.1016/j.jmrt.2020.09.079
27. Karandikar, P.G.; Evans, G.; Wong, S.; Aghajanian, M.K. A Review of Ceramics for Armor Applications. In *Advances in Ceramic Armor IV*; John Wiley & Sons: Hoboken, NJ, USA, 2008; pp. 163–178.
28. Medvedovski, E. Ballistic performance of armour ceramics: Influence of design and structure. Part 2. *Ceramics International* **2010**, *36*, 2117–2127. https://doi.org/10.1016/j.ceramint.2010.04.002
29. Crouch, I.G. Body armour–New materials, new systems. *Defence Technology* **2019**, *15*, 241–253. https://doi.org/10.1016/j.dt.2019.02.002
30. Krishnan, S.V.; Binoj, J.S.; Mansingh, B.B.; Babu, N.H.; Palanisamy, D. Technical review: Improvement of mechanical properties and suitability towards armor applications–Alumina composites. *Ceramics International* **2021**, *47*, 23693–23701. https://doi.org/10.1016/j.ceramint.2021.05.097
31. Medvedovski, E. Lightweight ceramic composite armour system. *Advances in Applied Ceramics* **2006**, *105*, 241–245. https://doi.org/10.1179/174367606X113563
32. Chabera, P.; Boczkowska, A.; Lindemann, Z. Comparison of numerical and experimental study of armour system based on alumina and silicon carbide ceramics. *Bulletin of the Polish Academy of Sciences: Technical Sciences* **2015**, *63*, 363–367. https://doi.org/10.1515/bpasts-2015-0041
33. Flinders, M.; Ray, D.; Anderson, A.; Cutler, R.A. High-toughness silicon carbide as armor. *Journal of the American Ceramic Society* **2005**, *88*, 2217–2226. https://doi.org/10.1111/j.1551-2916.2005.00415.x
34. Muhammad, R.; Ali, M.; Khan, M.A.; Iqbal, M.A. Computational investigation of the dynamic response of silicon carbide ceramic under impact loading. *Materials Research Express* **2022**, *9*, 095204. https://doi.org/10.1088/2053-1591/ac8e3a
35. Abdul H.M.H.; Abd-Ali, N.K. Analysis of the mechanical behavior of carbon-kevlar-glass fiber reinforced composite with silicon carbide. *AIP Conference Proceedings* **2024**, *2897*, 020003. https://doi.org/10.1063/5.0194864
36. Nair, A.N.; Sundharesan, S.; Al Tubi, I.S.M. Kevlar-based composite material and its applications in body armour: a short literature review. In *IOP Conference Series: Materials Science and Engineering*; IOP Publishing: Bristol, UK, 2020; Volume 923, pp. 012053. https://doi.org/10.1088/1757-899X/923/1/012053
37. Octavian, J.; Simona, L. Ballistic performance of monolithic rubber-ceramic composite armor. *Journal of Composite Materials* **2024**, *58*, 689–706. https://doi.org/10.1177/00219983241231692
38. National Institute of Justice (NIJ). Ballistic Resistance of Body Armor, NIJ Standard-0101.03. U.S. Department of Justice: Washington, DC, USA, 1987.

39. Cronin, D.S.; Bui, K.; Kaufmann, C.; McIntosh, G.; Berstad, T. Implementation and validation of the Johnson-Holmquist ceramic material model in LS-Dyna. Proceedings of the 4th European LS-DYNA Users Conference; Ulm, Germany, May 22–23, 2003; pp. 1–10.
40. Hiermaier, S.; Riedel, W.; Sauer, M.; Stilp, A. *Advanced Material Models for Hypervelocity Impact Simulations*. ESA/ESTEC: Paris, France, 1999.
41. Malik, O.A.; Khan, H.A. Impact resistance analysis using multiply fabric orientations. In *Proceedings of the 2015 Fourth International Conference on Aerospace Science and Engineering (ICASE)*; Islamabad, Pakistan, December 14–16 2015; IEEE: Piscataway, NJ, USA, 2015; pp. 1–6.
42. Shen, R.; Chen, Y.; Liu, H.; Zhang, D. An enhanced vacuum-assisted resin transfer molding process and its pressure effect on resin infusion behavior and composite material performance. *Polymers* **2024**, *16*, 1386. https:/ /doi.org/10.3390/polym16101386
43. Liu, T.; Wang, X.; Chen, L.; Zhang, Y. Improved laser measurement using advanced techniques: A review. *Microwave and Optical Technology Letters* **2022**, *64*, 2256–2263. https://doi.org/10.1002/mop.33408
44. Cepuš, E. An Experimental Investigation of the Early Dynamic Impact Behaviour of Textile Armour Systems: Decoupling Material from Structural Effects. Ph.D. Thesis, University of British Columbia: Vancouver, BC, Canada, 2003.
45. Kılıç, N.; Ekici, B. Ballistic resistance of high hardness armor steels against 7.62 mm armor piercing ammunition. *Materials & Design* **2013**, *44*, 35–48. https://doi.org/10.1016/j.matdes.2012.07.028
46. Feli, S.; Asgari, M. Finite element simulation of ceramic/composite armor under ballistic impact. *Composites Part B: Engineering* **2011**, *42*, 771–780. https://doi.org/10.1016/j.compositesb.2011.01.026
47. Livermore Software Technology Corporation (LSTC*). LS-DYNA Keyword User's Manual (Version 971)*. Livermore: CA, USA, 2014.
48. Johnson, G.R.; Cook, W.H. A constitutive model and data for metals subjected to large strains, high strain rates and high temperatures. In *Proceedings of the 7th International Symposium on Ballistics*; The Hague, The Netherlands, April 19–21 1983; pp. 541–547.
49. Hallquist, J.O. *LS-DYNA3D Theoretical Manual*. Livermore Software Technology Corporation: Livermore, CA, USA, 1993.
50. Holmquist, T.J.; Templeton, D.W.; Bishnoi, K.D. Constitutive modeling of aluminum nitride for large strain, high-strain rate, and high-pressure applications. *International Journal of Impact Engineering* **2001**, *25*, 211–231. https://doi.org/10.1016/S0734-743X(00)00049-5
51. Johnson, G.R.; Holmquist, T.J.; Beissel, S.R. An improved computational constitutive model for brittle materials. *AIP Conference Proceedings* **1994**, *309*, 981–984. https://doi.org/10.1063/1.46461
52. Wang, J.; Li, X.; Zhang, Y. Simulation research on cutting brittle optical material with diamond wire saw based on LS-DYNA. In *Proceedings of the 7th International Symposium on Advanced Optical Manufacturing and Testing Technologies (AOMATT 2014)*; Harbin, China, April 26–29 2014; SPIE: Bellingham, WA, USA, 2014; Volume 9281, p. 92810D.
53. Bresciani, L.M.; Manes, A.; Giglio, M. Numerical modelling to reproduce fragmentation of a tungsten heavy alloy projectile impacting a ceramic tile: Adaptive solid mesh to the SPH technique and the cohesive law. *International Journal of Impact Engineering* **2016**, *87*, 3–13. https://doi.org/10.1016/j.ijimpeng.2015.09.001
54. Hiermaier, S.; Riedel, W.; Sauer, M. *Advanced Material Models for Hypervelocity Impact Simulations*. Fraunhofer EMI: Freiburg, Germany, 1999.
55. Anderson, C.E.; Cox, P.A.; Johnson, G.R.; Maudlin, P.J. A constitutive formulation for anisotropic materials suitable for wave propagation computer programs—II. *Computational Mechanics* **1994**, *15*, 201–223. https://doi.org/10.1007/BF00376734
56. Strassburger, E.; Senf, H.; Rothenhäusler, H. Fracture propagation during impact in three types of ceramics. *Le Journal de Physique IV* **1994**, *4*, C8-653–C8-658. https://doi.org/10.1051/jp4:19948100
57. Hetherington, J.G. The optimization of two component composite armours. *International Journal of Impact Engineering* **1992**, *12*, 409–414. https://doi.org/10.1016/0734-743X(92)90167-2
58. Cristescu, N.; Malvern, L.E.; Sierakowski, R.L. Failure mechanisms in composite plates impacted by blunt-ended penetrators. In *Foreign Object Impact Damage to Composites*; ASTM International: West Conshohocken, PA, USA, 1975; pp. 159–172.

Publisher's Note: IIKII stays neutral with regard to jurisdictional claims in published maps and institutional affiliations.

© 2025 The Author(s). Published with license by IIKII, Singapore. This is an Open Access article distributed under the terms of the Creative Commons Attribution License (CC BY), which permits unrestricted use, distribution, and reproduction in any medium, provided the original author and source are credited.